buildings

MDPI

Article

Stress–Strain Relationship of C-Shaped Steel Tube-Confined Concrete Under Axial Compression

Xuan Mo [1], Dan Liang [1,*], Tengfei Zhao [2], Le Zhang [1] and Cuicui Wu [1]

[1] Jiangxi Vocational College of Finance & Economics, Jiujiang 332000, China
[2] College of Urban Construction, Jiangxi Normal University, Nanchang 330000, China
* Correspondence: ld@jxvc.edu.cn

Abstract

Axial compression tests were conducted on four groups of C-shaped steel tube-confined concrete specimens. The results demonstrate that the C-shaped steel tube effectively confines the core concrete, significantly enhancing the peak compressive stress by 14.1% to 22.1% compared to unconfined concrete, resulting in a more gradual descending branch of the stress–strain curve, and effectively improving the ultimate deformation capacity of the concrete with peak strain increasing by a factor of 1.45 to 1.68. The influences of steel plate thickness and reinforcement on the compressive stress–strain curve of the confined concrete were systematically analyzed. Based on the analysis of the strain in the steel tube and the stress state of the confined concrete during testing, a method for calculating the effective confining stress on the core concrete is proposed. A uniaxial compressive stress–strain model for C-shaped steel tube-confined concrete is developed based on the Mander model. Comparisons show that the proposed model agrees well with the experimental stress–strain curves, with predicted peak stresses within 5% of experimental values and predicted peak strains within 7% deviation.

Keywords: composite shear wall; C-shaped steel tube; confined concrete; stress–strain relationship

1. Introduction

Under horizontal cyclic loading, the failure mode of medium-high C-shaped steel frame composite shear walls typically manifests as concrete crushing in the frame regions at both ends, coupled with poor ultimate deformation capacity of the shear walls and a pronounced buckling propensity of C-shaped steel flanges. To preclude the premature crushing of frame concrete and improve the stability of C-shaped steel flanges, densified reinforcement is disposed along the direction of the C-shaped steel frame to connect the flange plates, thereby forming steel hoops. By virtue of the confinement provided by the steel hoops to the concrete, the bearing capacity and ultimate deformation capacity of concrete in these regions are enhanced, which in turn improves the deformation and energy dissipation capacities of the C-shaped steel frame composite shear walls. Owing to constraints on the number of tests and research funding, extensive research on such shear walls must rely on finite element numerical simulation methods. Determining the stress–strain relationship of confined concrete inside the steel hoops in the finite element model constitutes the primary challenge to be addressed.

Compared with stirrup-confined core concrete, steel tube confinement offers the advantage of continuous and closed steel plates, providing continuous and stronger effective

Check for updates

Academic Editor: Eugeniusz Koda

Received: 5 April 2026
Revised: 19 April 2026
Accepted: 23 April 2026
Published: 1 May 2026

Copyright: © 2026 by the authors. Licensee MDPI, Basel, Switzerland. This article is an open access article distributed under the terms and conditions of the Creative Commons Attribution (CC BY) license.

confinement to the core concrete. Extensive research has been conducted on various types of concrete-filled steel tube (CFST) columns [1–5]. The general approach for the stress–strain relationship of confined concrete is often based on the Mander constitutive model [6,7], determining confinement coefficients through regression of test results, and finally proposing an equivalent uniaxial stress–strain model for CFST columns. Tube-confined concrete columns have also been widely studied. Tomii et al. [8] first proposed the concept and investigated the seismic performance of tube-confined columns. Zhang Sumei et al. [9] conducted experiments and analysis on confined circular high-strength CFST stub columns. Their results indicated that when the steel tube does not carry axial load, its confinement on the core concrete is more effective. For high-strength concrete, the peak strain calculated by the Mander model was significantly higher than the test results. Zhou Xu hong [10] tested 20 square steel tube-confined concrete short columns. Comparing load–displacement curves under different concrete strengths and width-to-thickness ratios revealed that ductility decreased with increasing concrete strength and width-to-thickness ratio. Gao Long [11] designed a rectangular steel tube with three steel plates and one lacing plate, conducting axial monotonic loading tests. The results showed significant improvements in the peak stress and peak strain of the core concrete, verifying effective confinement. Compared with plain concrete, the descending branch of the stress–strain curve was more gradual, and ductility was significantly enhanced. Based on stress state analysis and the Mander model, a stress–strain calculation model for rectangular steel tube-confined concrete was proposed. Numerous constitutive models have been proposed for confined concrete in different CFST columns, such as Sargin, Saenz, Kent–Park, Popovics, Attard & Setunge, and Han Linhai's CFST model [12–17]. Furthermore, Hany, Lu, Shirmohammadi, Ziaadiny, and Afifi, among others [18–22], have studied FRP-confined concrete and proposed corresponding stress–strain models.

Unlike CFST with four-sided steel plates, this study focuses on a steel tube with three steel plates and one side of reinforcement. The author designed four independent groups of steel tube-confined concrete specimens for axial compression tests. The test results indicate that the presence of reinforcement and increased plate thickness enhances the peak stress by up to 21% and peak strain by up to 68% relative to plain concrete. Based on the analysis of test and finite element results, and drawing upon the Mander model and research findings for square CFST columns, a uniaxial compressive stress–strain calculation method is proposed for the three-plate, one-reinforcement-side steel tube-confined concrete. The proposed model demonstrates high accuracy in predicting the full-range behavior, thereby providing a reliable constitutive basis for the nonlinear finite element analysis of composite shear walls incorporating C-shaped steel boundary elements.

2. Experimental Study

2.1. Specimen Design

Considering that the C-shaped steel border and its enclosed concrete in a composite shear wall (Figure 1) primarily resist axial compression under combined axial and lateral loads, this study designed four groups of independent steel tube-confined concrete specimens (GTT1-GTT4). Each group contained three identical specimens to investigate the confinement effect. GTT1 consisted of three steel plates without reinforcement. GTT2, GTT3, and GTT4 consisted of three steel plates with one side of reinforcement. The internal concrete dimensions for GTT1-GTT3 were 147 mm × 144 mm × 300 mm, and for GTT4 were 138 mm × 138 mm × 300 mm. Steel plates were cold-bent into a C-shape. Notches were pre-cut within 10 mm from the top and bottom edges for subsequent removal. Reinforcement was bent and welded directly to the steel plate side walls. Specimen geometry

and details are shown in Figure 2. All materials, including the Q235B steel plates, HRB400 reinforcement, and C40 concrete, were sourced from Guangdong, China.

The design strength for the concrete inside the tubes was C40. During the casting of GTT1-GTT4, three standard concrete cubes were also cast. All specimens and cubes were cured under identical conditions for 28 days. On the testing day for GTT1-GTT4, the reserved cubes were tested axially to determine the average compressive strength. Steel plates were Q235B, and reinforcement was HRB400. Following GB/T 2975-2018 [23], three standard tensile coupons for steel plates and three for reinforcement were prepared. Tensile tests were conducted according to GB/T 228.1-2010 [24] to determine the yield strength, ultimate strength, and elastic modulus of the steel plates and reinforcement. Material properties are listed in Table 1.

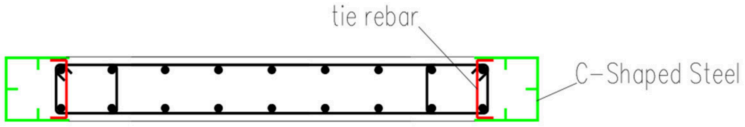

Figure 1. Schematic section of C-shaped steel border composite shear wall.

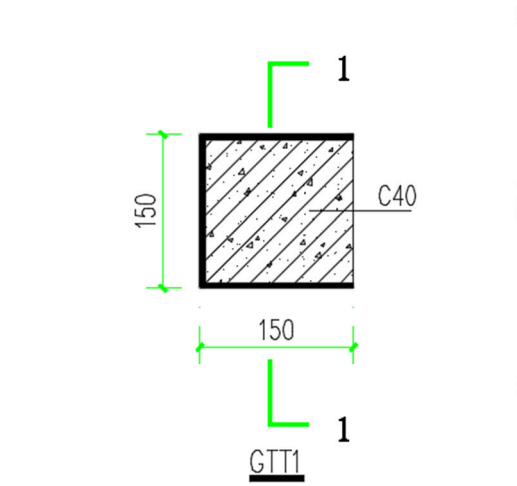

(**a**) GTT1

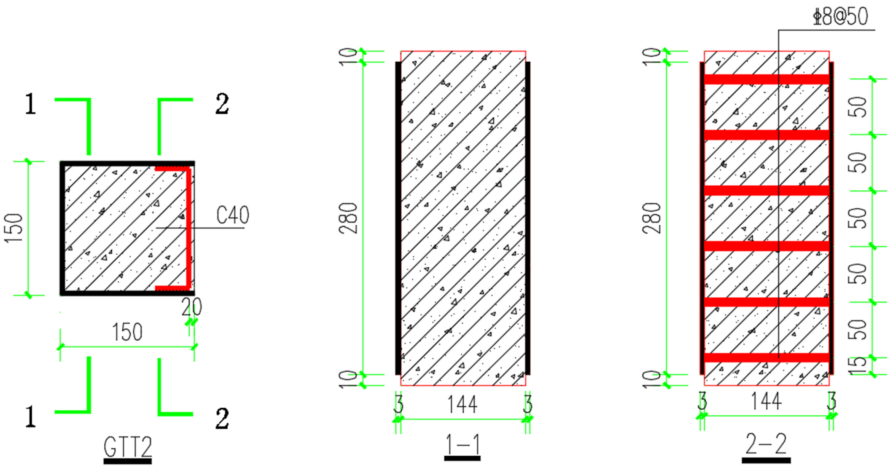

(**b**) GTT2

Figure 2. *Cont.*

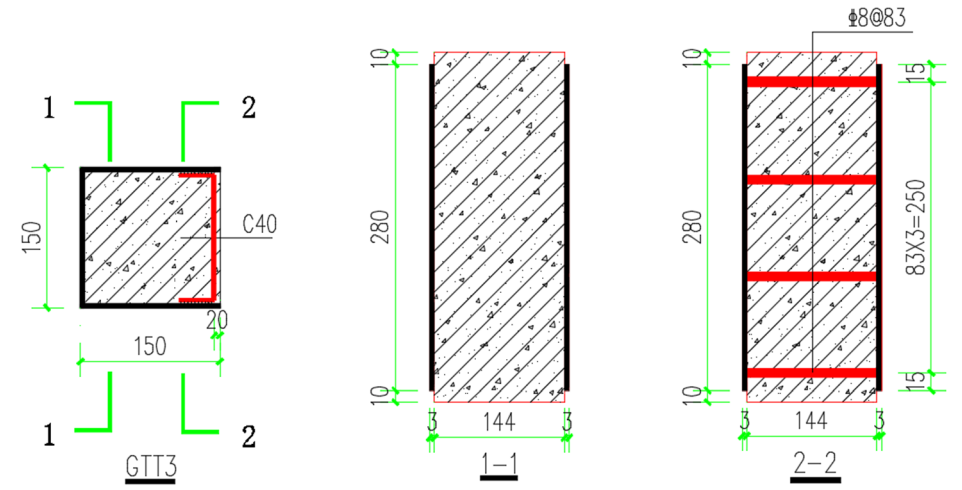

(**c**) GTT3

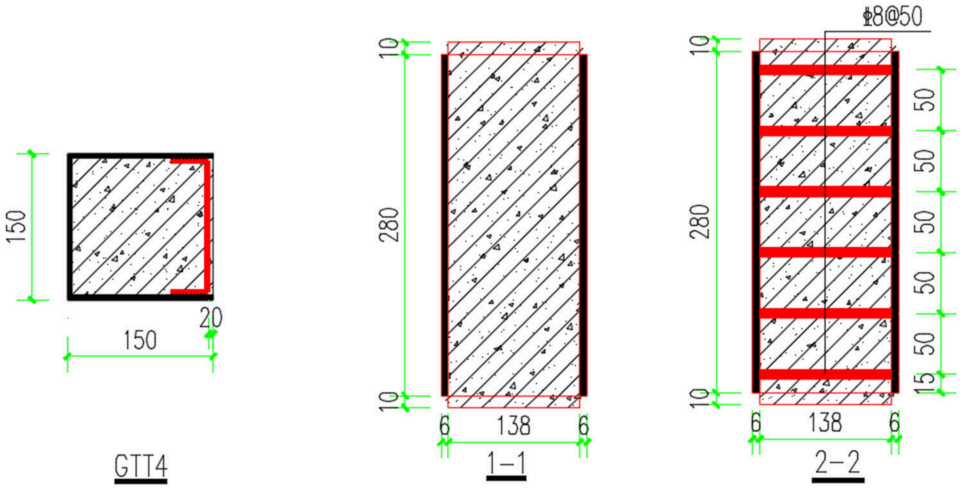

(**d**) GTT4

Figure 2. Specimen geometry and construction.

Table 1. Material mechanical properties.

Concrete Cube Strength (MPa)	Steel Plate (2.86 mm/6 mm)			Reinforcement		
	Yield Strength (MPa)	Ultimate Strength (MPa)	Elastic Modulus (GPa)	Yield Strength (MPa)	Ultimate Strength (MPa)	Elastic Modulus (GPa)
43	267/258	417/426	201/203	416	602	195

2.2. Test Setup and Instrumentation

As the C-shaped steel border is located at the structural boundary elements, its stress state is close to uniaxial compression/tension. All specimens were tested under axial monotonic compression using a 2000 kN universal testing machine (Lshi Instruments Co., Ltd., Shanghai, China) in accordance with GB/T 50081-2019 "Standard for test methods of concrete physical and mechanical properties" [25]. Before testing, the 10 mm high steel plate sections at both ends were removed to prevent direct axial load on the steel plates. Loading was controlled by both force and displacement. Force control was used initially: increments of 100 kN below 400 kN, and 50 kN between 400 and 700 kN. Beyond 700 kN, displacement control was applied at 0.3 mm/min until a maximum displacement of 6 mm. The test setup is shown in Figure 3.



Figure 3. Test setup.

Measured parameters included: axial load, axial deformation, transverse and longitudinal strains on the steel plates, and strain in the reinforcement. Strain gauges were attached at the mid-height of the reinforcement. The layout of strain gauges on the steel plates is shown in Figure 4. Axial load was recorded by the testing machine. Axial displacement was measured by two linear variable differential transformers (LVDTs). Strains in the steel plates and reinforcement were recorded using a DH3815 static strain data acquisition system (Jiangsu Donghua Testing Technology Co., Ltd., Jingjiang, China).

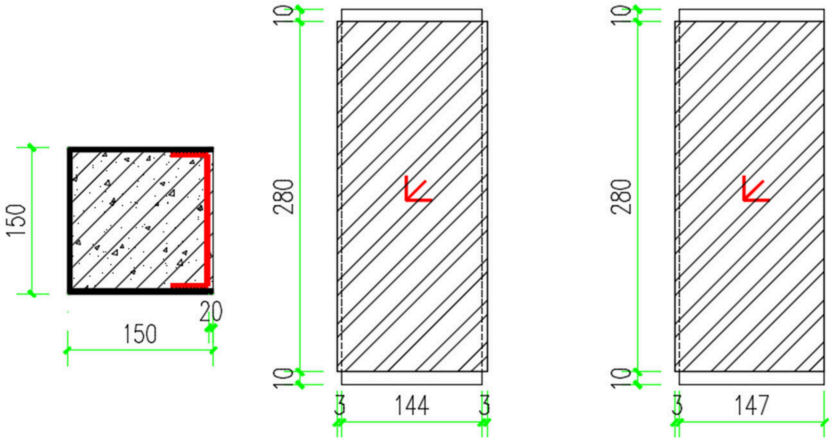

Figure 4. Strain gauge layout.

3. Test Results and Analysis

3.1. Test Observations

GTT1: During initial loading, the specimen remained elastic with no visible cracks. At 879 kN, several hairline-thick (approximately 0.05–0.1 mm in width) fine vertical cracks, ranging from 30 mm to 60 mm in length, appeared on the concrete surface without a steel plate (open side). These cracks initiated near the mid-height region and propagated vertically upward and downward. Initially, the cracks were isolated from each other without branching. After reaching the peak load of 940 kN, the load began to drop. One of the initial fine vertical cracks progressively widened and extended, eventually forming a penetrating vertical crack near the mid-height on the open side, accompanied by the spalling of concrete in the mid-lower region. The spalled concrete fragments exhibited a rough, grainy texture characteristic of brittle tensile fracture of the cement matrix, with the maximum spall depth measured at approximately 18 mm. Subsequently, the corner concrete

spalled off. With increasing displacement, the flange plates bulged outward noticeably. At 4.74 mm displacement, conical spalling occurred on the open side. The failure mode resembled that of a plain concrete prism under end restraint ("hoop effect"). The specimen was severely damaged at the end of testing. Failure mode is shown in Figure 5.

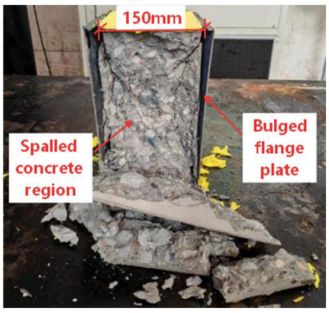

Figure 5. GTT1 failure mode.

GTT2: Compared to GTT1, GTT2 had reinforcement (8 mm diameter @50 mm spacing) on the open side, enhancing confinement. Initial behavior was similar to GTT1. At 950 kN, fine vertical cracks appeared in the middle of the reinforced side. After peaking at 1017 kN, the load decreased. Vertical cracks developed at the top of the reinforced side, evolving into inclined cracks. Non-penetrating vertical cracks formed near the mid-height. Concrete spalling occurred at the top, exposing some reinforcement. Spalling was more severe at the edges than in the middle. At 5.11 mm displacement, concrete at the top of the reinforced side completely spalled off, fully exposing the reinforcement (which remained connected to the plates). No significant deformation of the steel plates was observed. The specimen was severely damaged. Failure mode is shown in Figure 6.



(**a**) cracking stage (**b**) failure stage

Figure 6. GTT2 failure progression.

GTT3: Compared to GTT2, GTT3 had a larger reinforcement spacing (83 mm). Initial behavior was similar. At 932 kN, fine vertical cracks appeared in the lower part of the reinforced side, and slight local buckling occurred at the plate ends (but without detachment from concrete). After peaking at 996 kN, the load dropped. Corner concrete spalled on the reinforced side, and vertical cracks appeared in the middle. At 3.5 mm displacement, concrete in the middle of the reinforced side crushed and spalled, and significant bulging occurred in the middle of the steel plates. At 4.78 mm displacement, concrete at the top of the reinforced side completely spalled, exposing reinforcement (still connected). The specimen was severely damaged. Failure mode is shown in Figure 7.

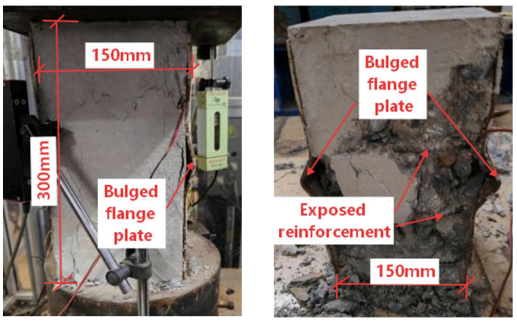

(**a**) cracking stage (**b**) failure stage

Figure 7. GTT3 failure progression.

GTT4: Compared to GTT2, GTT4 had the same reinforcement layout but thicker steel plates (6 mm). Initial behavior was similar. At 944 kN, multiple fine vertical cracks appeared in the middle of the reinforced side. These cracks showed little change with increasing load. After peaking at 1049 kN, the load decreased. Corner concrete spalled on the reinforced side, and one of the initial fine vertical cracks progressively widened and extended to form a penetrating vertical crack in the middle, with local concrete bulging (but no spalling). At 3.7 mm displacement, concrete in the mid-lower part of the reinforced side spalled, partially exposing reinforcement. At 5.48 mm displacement, concrete in the mid-lower part of the reinforced side completely spalled, fully exposing the reinforcement (still connected). No significant deformation of the steel plates was observed. The specimen was severely damaged. Failure mode is shown in Figure 8.

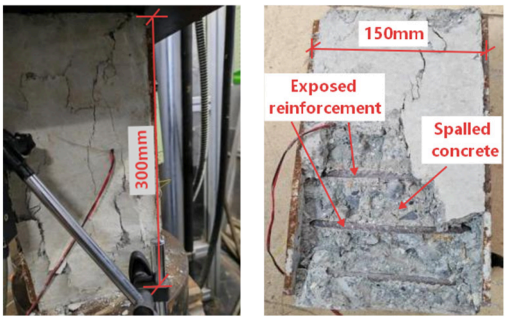

(**a**) cracking stage (**b**) failure stage

Figure 8. GTT4 failure progression.

3.2. Load–Displacement Curves

Peak loads and corresponding displacements for the four groups are listed in Table 2 (one GTT1 specimen was discarded due to significant deviation). Results indicate good consistency within each group. The average of the three specimens is taken as the representative result.

Load–displacement curves for GTT1–GTT4 are shown in Figure 9. To illustrate the confinement effect, the stress–strain curve of plain concrete is compared with that of the confined concrete specimens in Figure 10. The standard cube strength was converted to the axial compressive strength according to GB 50010-2010 (2015 edition) [26]. The peak strain for plain concrete was taken as 1826×10^{-6} via linear interpolation. The plain concrete stress–strain curve was derived based on the code. The load–displacement curves of GTT1–GTT4 were converted to stress–strain curves. The specimens with reinforcement (GTT2–GTT4) showed similar ascending branches up to the peak load. Specimens with thicker plates and closer reinforcement spacing exhibited a more gradual descending

branch, while those with larger reinforcement spacing showed a steeper initial descent. The observed increase in peak strain for GTT2 (1.68 times that of plain concrete) is consistent with the range reported by Zhou et al. [10] for square steel tube-confined concrete (typically 1.5 to 2.0 times), confirming that the addition of reinforcement effectively compensates for the open side's lack of confinement.

Table 2. Peak displacement and peak load of specimens.

Group	Specimen ID	Peak Disp. (mm)	Average (mm)	Peak Load (kN)	Average (kN)
1 (GTT1)	A B	0.77 0.81	0.79	852.6 865.2	858.9
2 (GTT2)	A B C	1.43 1.30 1.32	1.35	1017.3 1006.5 1001.6	1008.5
3 (GTT3)	A B C	1.29 1.32 1.38	1.33	966.8 996.96 971.3	978.4
4 (GTT4)	A B C	1.46 1.51 1.62	1.53	1039.8 1037.2 1058.7	1042.2

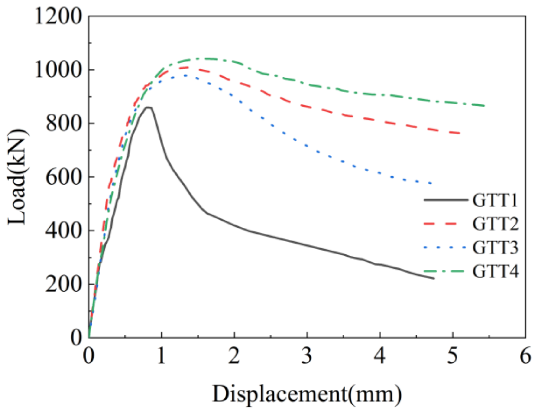

Figure 9. Load–displacement curves.

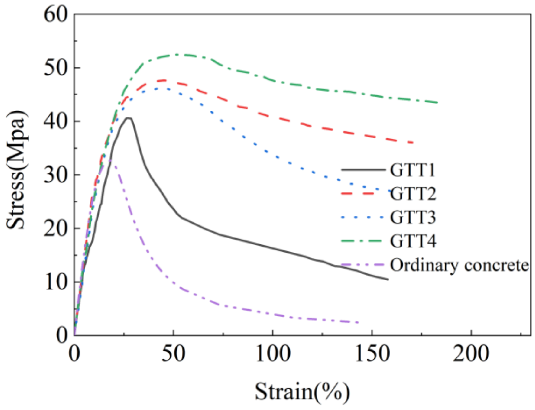

Figure 10. Stress–strain curves.

3.3. Stress Analysis

To investigate the confinement mechanism and its evolution during loading, the relationship between the strains in the steel plates/reinforcement and the axial load was analyzed, as shown in Figure 11. Stresses were calculated from strains using Hooke's law, and their relationship with axial load is shown in Figure 12.

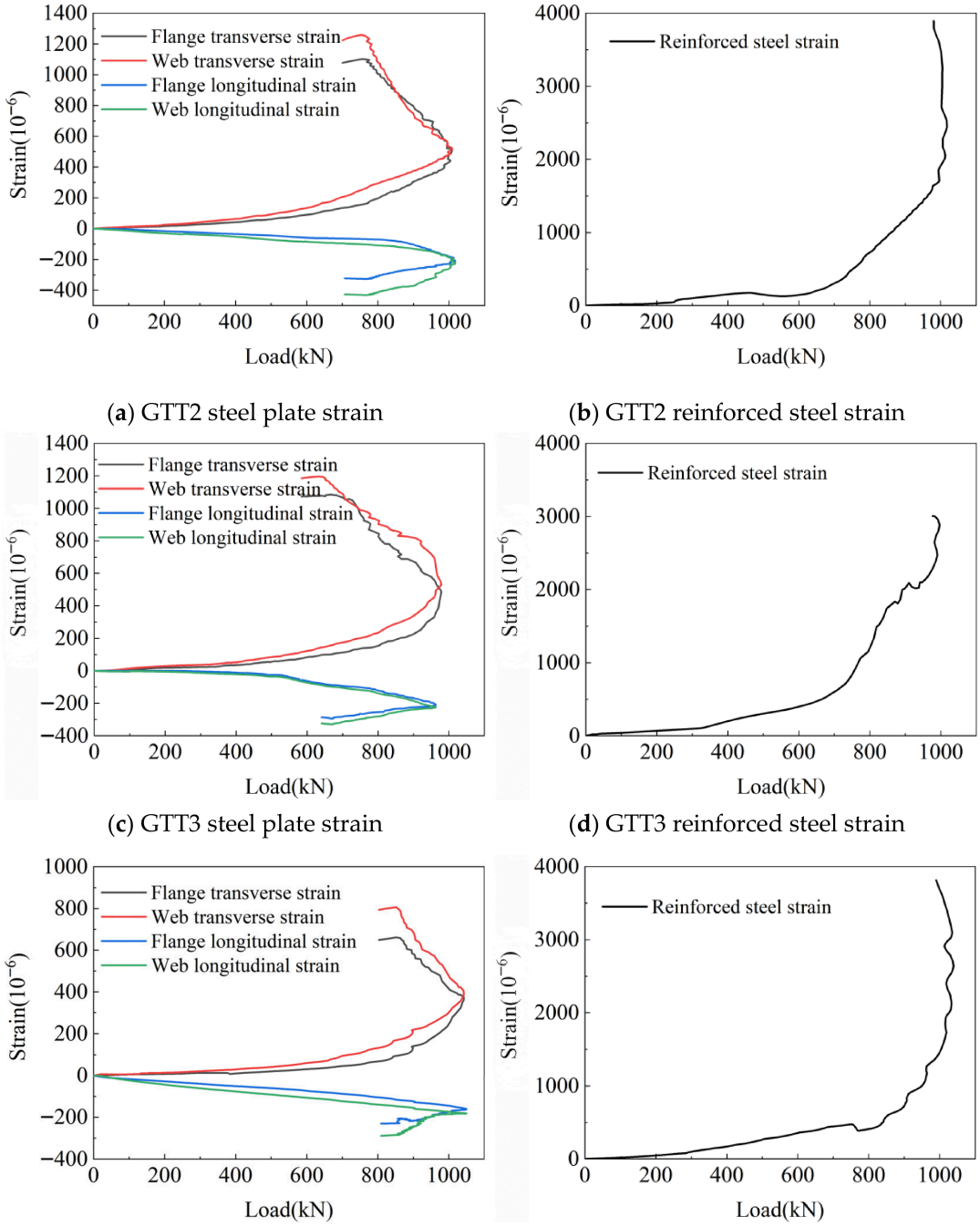

(**a**) GTT2 steel plate strain (**b**) GTT2 reinforced steel strain

(**c**) GTT3 steel plate strain (**d**) GTT3 reinforced steel strain

(**e**) GTT4 steel plate strain (**f**) GTT4 reinforced steel strain

Figure 11. GTT2-GTT4 strain–load curve.

The results show that the stresses in the flange and web plates for GTT2 and GTT3 were similar. Compared to GTT2, the flange plate stress in GTT4 decreased by 25.5%, and the web plate stress decreased by 23.7%. For all specimens GTT2-GTT4, the steel plates did not yield before the peak load was reached. However, the axial load–strain curves for the reinforcement in GTT2-GTT4 indicate that the reinforcement yielded before the peak load was attained.

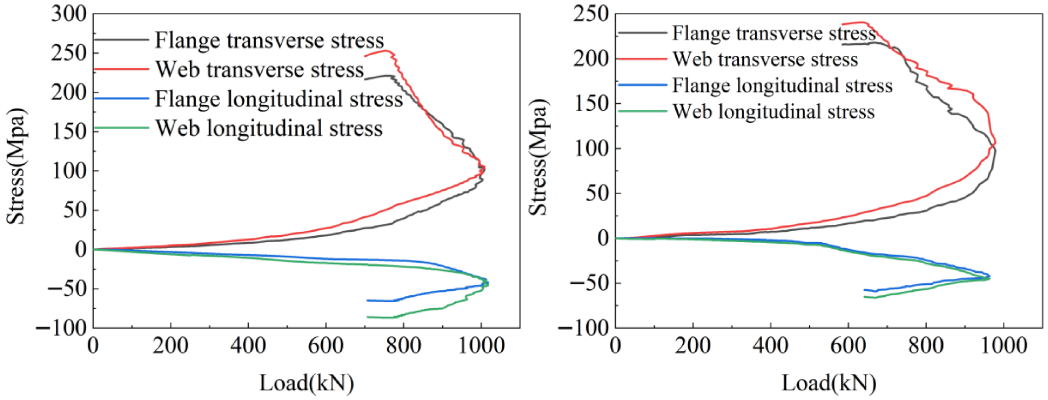

(**a**) GTT2 steel plate stress

(**b**) GTT3 steel plate stress

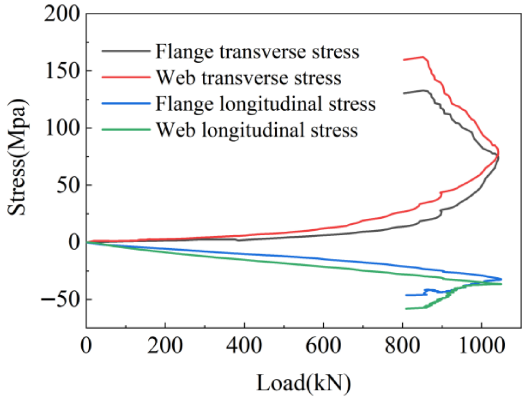

(**c**) GTT4 steel plate stress

Figure 12. GTT2-GTT4 stress–load curve.

4. Stress–Strain Relationship for Confined Concrete

4.1. Basic Equations

Confined concrete exhibits enhanced peak stress, peak strain, and ductility compared to plain concrete. The Mander model, developed for stirrup-confined concrete, is expressed by Equations (1)–(6). Mander's tests showed that stirrups yielded before the peak load, and their stress continued to increase slightly in the descending branch. For structural safety, Mander assumed the effective confining stress remains constant in the descending branch.

The Mander model is selected as the foundational framework for this study due to its distinct advantages over other widely used confined concrete models (e.g., Kent–Park, Popovics, or Han's model). Specifically, the Mander model explicitly accounts for the effective confinement area and the non-uniform lateral confining pressures through the confinement effectiveness coefficient. Unlike models that are purely empirical regression fits for specific tube shapes, the Mander framework allows for a clear separation of the steel tube's geometric contribution and the material's lateral response. This feature makes it highly adaptable to the unique C-shaped cross-section with a discontinuous reinforcement side investigated herein, where the confining stress distribution is inherently non-uniform and asymmetrical.

$$f_c = \frac{f_{cc} x r}{r - 1 + x^r} \tag{1}$$

$$f_{cc} = f_{co}\left(-1.254 + 2.254\sqrt{1 + 7.94\frac{f_1}{f_{co}}} - 2\frac{f_1}{f_{co}}\right) \tag{2}$$

$$\varepsilon_{cc} = \varepsilon_{co}[1 + 5(\frac{f_{cc}}{f_{co}} - 1)] \tag{3}$$

$$x = \frac{\varepsilon_c}{\varepsilon_{cc}} \tag{4}$$

$$r = \frac{E_c}{E_c - E_{\text{sec}}} \tag{5}$$

$$E_{\text{sec}} = \frac{f_{cc}}{\varepsilon_{cc}} \tag{6}$$

where f_c is the stress of the confined concrete; f_{cc} is the peak stress of the confined concrete; f_{co} is the peak stress of the plain concrete; f_1 is the effective lateral confining stress; ε_c is the strain of the confined concrete; ε_{cc} is the peak strain of the confined concrete; and ε_{co} is the peak strain of the plain concrete.

From these equations, determining the effective lateral confining stress f_1 is key to obtaining the peak stress f_{cc}. Since the lateral confining stresses from the C-shaped tube are unequal in the two principal directions, the effective lateral confining stress can be determined using the effective confinement coefficient and the lateral confining stresses [10]:

$$f_1 = k_e f_1' \tag{7}$$

where f_1' is the lateral confining stresses, and k_e is the effective confinement coefficient.

4.2. Effective Confinement Coefficient

The effective confinement coefficient is defined as [10]:

$$k_e = \frac{A_e}{A_c} \tag{8}$$

where A_e is the effectively confined core concrete area, and A_c is the total core concrete area.

Referring to [10], the assumed confinement model for concrete confined by a square steel tube is shown in Figure 13. The effectively confined area is shown with cross-hatching. The ineffectively confined zones are assumed to initiate at 0.1 D from the corners and develop along parabolic arcs to points 0.1 D from the opposite corners, with the parabola's initial tangent at 45°. Assuming a similar confinement model applies to the C-shaped tube-confined specimens, the effectively confined area is shown in Figure 14.

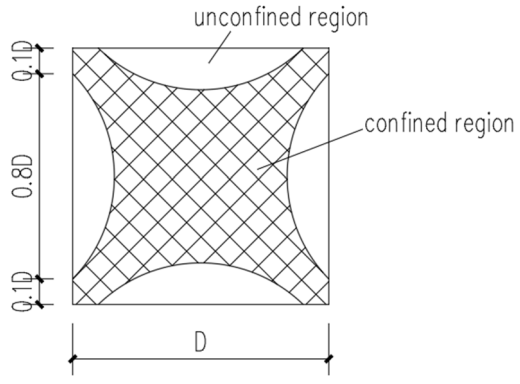

Figure 13. Square steel tube confinement model.

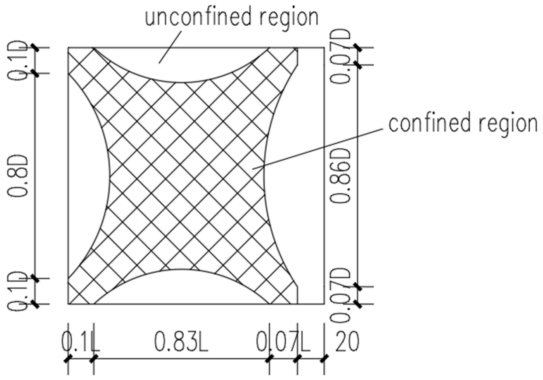

Figure 14. GTT confinement model.

To validate the assumed effectively confined area for the C-shaped tube, a finite element model of GTT2 was established using ABAQUS 2020. Steel plates were modeled with S4R shell elements, concrete with C3D8R solid elements, and reinforcement with T3D2R truss elements. Based on test observations showing no separation, the steel plates and reinforcement were merged. Surface-to-surface contact was defined between the steel tube and concrete: tangential behavior with a penalty friction coefficient of 0.2, and normal behavior as "hard" contact. Reinforcement elements were embedded into the concrete. A reference point was coupled to the top surface of the core concrete, and an axial displacement was applied to this point. The bottom surface was fixed in the axial direction. The model is shown in Figure 15.

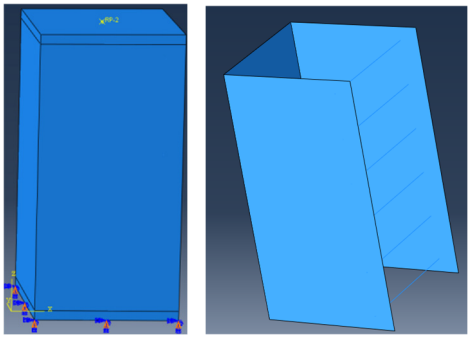

Figure 15. Finite element model of GTT2.

Figure 16 shows the principal stress contours at peak load. It can be observed that the confinement is strongest near the corners of the steel plate sides. The confinement near the corners of the reinforced side is slightly weaker than the plate sides. The mid-regions of all sides have weaker confinement, with the middle of the reinforced side being the weakest. This pattern is generally consistent with the assumed model in Figure 14, validating the rationality of the assumed effectively confined area.

Based on the geometry in Figure 14, the expression for the effective confinement coefficient k_e is derived as:

$$k_e = L \times D - 0.197\left(L^2 + D^2\right) \tag{9}$$

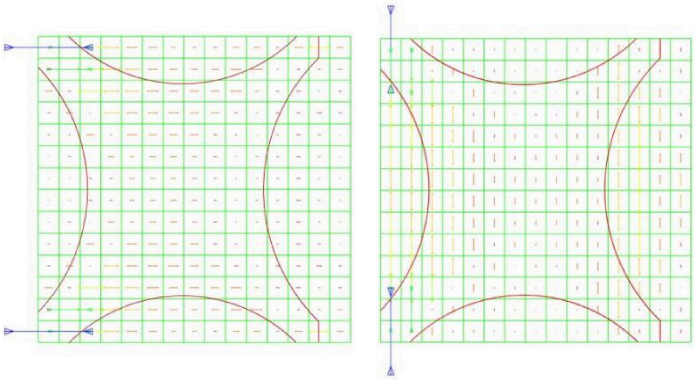

(**a**) X-direction (**b**) Y-direction

Figure 16. Principal stress contours at peak load.

4.3. Effective Confining Stress

Since the lateral confining stresses f'_{1x} and f'_{1y} are unequal, the effective lateral confining stress f'_1 on the core concrete lies between them, f'_{1x} and f'_{1y} are related to the reinforcement spacing, diameter, and the thickness of the C-shaped steel plates. Coefficients η_x and η_y are introduced to represent the contribution of the confining stresses from the two directions to the core concrete. The proposed expression for the effective lateral confining stress is given by Equations (10)–(13):

$$f'_1 = \eta_x f'_{1x} + \eta_y f'_{1y} \tag{10}$$

$$\eta_x + \eta_y = 1 \tag{11}$$

$$\eta_x = \frac{2t \cdot \sigma_{xh} \cdot s}{2t \cdot \sigma_{xh} \cdot s + t \cdot s \cdot \sigma_{yh} + f_y \cdot A_s} \tag{12}$$

$$\eta_y = \frac{t \cdot s \cdot \sigma_{yh} + f_y \cdot A_s}{2t \cdot \sigma_{xh} \cdot s + t \cdot s \cdot \sigma_{yh} + f_y \cdot A_s} \tag{13}$$

where f'_{1x} is the lateral confining stress in the x-direction; f'_{1y} is the lateral confining stress in the y-direction; η_x is the participation coefficient for the x-direction lateral confining stress; and η_y is the participation coefficient for the y-direction lateral confining stress.

A mechanical analysis of the steel tube is performed. The confining pressure provided by the steel tube to the concrete is non-uniform, as schematically shown in Figure 17. Based on static equilibrium, the average lateral confining stresses on the concrete are calculated as:

$$f'_{1x} = \frac{2t \cdot \sigma_{xh}}{D} \tag{14}$$

$$f'_{1y} = \frac{t \cdot s \cdot \sigma_{yh} + f_y \cdot A_s}{L \cdot s} \tag{15}$$

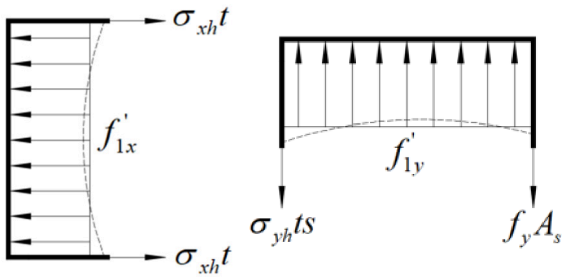

Figure 17. Mechanical analysis of the steel tube.

Based on the experimental stress analysis, the reinforcement yielded before the peak load. Considering structural safety, it is assumed that the stress in the reinforcement remains constant after yielding.

The steel plates did not yield at the peak load. It is assumed that the stress in the steel plates remains constant after the peak load. The relationship between the transverse stress in the steel plates at peak load and the width-to-thickness ratio D/t is shown in Figure 18. The results indicate that the transverse stress increases with the width-to-thickness ratio. Regression analysis based on the method in [10] yields the relationship between the transverse stress in the steel plates at the peak load of the specimen and the plate's width-to-thickness ratio, given by Equations (16) and (17).

$$\sigma_{xh} = 0.1(L/\mathrm{t})^{0.4} f_{215} \tag{16}$$

$$\sigma_{yh} = 0.1(D/\mathrm{t})^{0.4} f_{215} \tag{17}$$

where f_{215} is the design strength of Q235 steel.

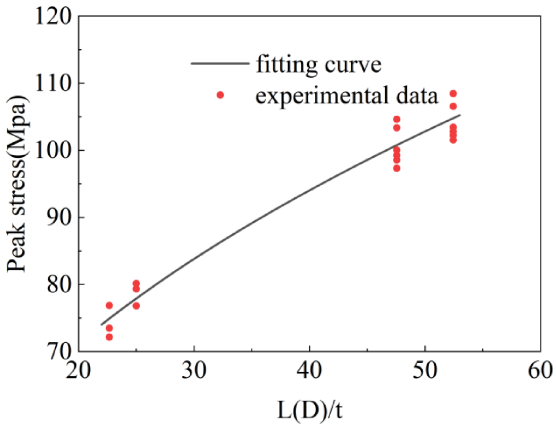

Figure 18. Fitting curve for peak stress vs. width-to-thickness ratio of steel plates in the tube.

4.4. Peak Strain

The Mander model was developed for stirrup-confined concrete, where the transverse reinforcement typically yields before the peak load, allowing substantial plastic dilation of the core concrete. The original Mander equation (Equation (3)) employs an enhancement coefficient of 5.0 for the peak strain. However, in the present study, the confinement is provided by C-shaped steel plates that, as shown in Figure 11, remain elastic at the peak load. This elastic confinement provides a stiffer lateral restraint that limits the axial strain development compared to yielded stirrups. Consequently, the peak strain enhancement observed in our tests is less pronounced than that predicted by the original Mander model. This finding aligns with the observations of Gao et al. [11] for rectangular steel tube-confined columns, where elastic plate confinement similarly resulted in a reduced enhancement coefficient. Regression analysis between the experimentally obtained peak strains and the calculated peak stresses is performed, as shown in Figure 19. Based on this analysis, the enhancement coefficient in Equation (3) is modified from 5.0 to 2.7 to better reflect the elastic confinement mechanism of the C-shaped steel tube. Equation (3) is thus modified to obtain the calculation expression for the peak strain of C-shaped steel tube-confined concrete, given by Equation (18).

$$\varepsilon_{cc} = \varepsilon_{co}[1 + 2.7(\frac{f_{cc}}{f_{co}} - 1)] \tag{18}$$

where the variables have the same meaning as in Equation (3).

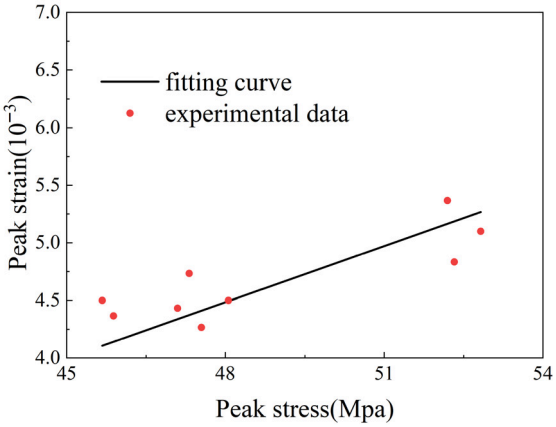

Figure 19. Fitting curve for peak strain vs. peak stress of tube-confined concrete.

5. Model Validation

The theoretical transverse stresses in the steel plates for GTT2-GTT4 are calculated using Equations (16) and (17) and compared with the experimental values in Table 3.

Table 3. Comparison of steel plate transverse stresses.

Tube Specimen ID	Location	Theoretical Value (MPa)	Experimental Value (MPa)	Ratio (Theo./Exp.)
GTT2	Flange	100.17	101.53	1.01
	Web	104.79	104.01	0.99
GTT3	Flange	100.17	100.83	1.00
	Web	104.79	102.79	0.98
GTT4	Flange	74.48	74.32	0.99
	Web	77.91	78.65	1.01

The calculated results are close to the experimental values, indicating the rationality of using Equations (16) and (17) to estimate the transverse stress in the steel plates.

To validate the proposed model, the theoretical stress–strain curves for GTT2-GTT4 are calculated using Equations (1), (2), (4)–(6) and (18). The procedure is as follows:

1. Calculate the effective confining stress f_1 using Equations (7)–(17).
2. Calculate the peak stress f_{cc} using Equation (2).
3. Calculate the peak strain ε_{cc} using Equation (18).
4. Calculate the stress–strain curve using Equations (1), (2), (4)–(6) and (18).

The calculated stress–strain curves for GTT2-GTT4 are compared with the experimental curves in Figure 20. The results show good agreement for both the ascending and descending branches of GTT2 and GTT4. For GTT3, the experimental descending branch is steeper than the theoretical prediction, likely due to the larger reinforcement spacing leading to local plate buckling, which reduced the confinement effectiveness and resulted in a sharper descent.

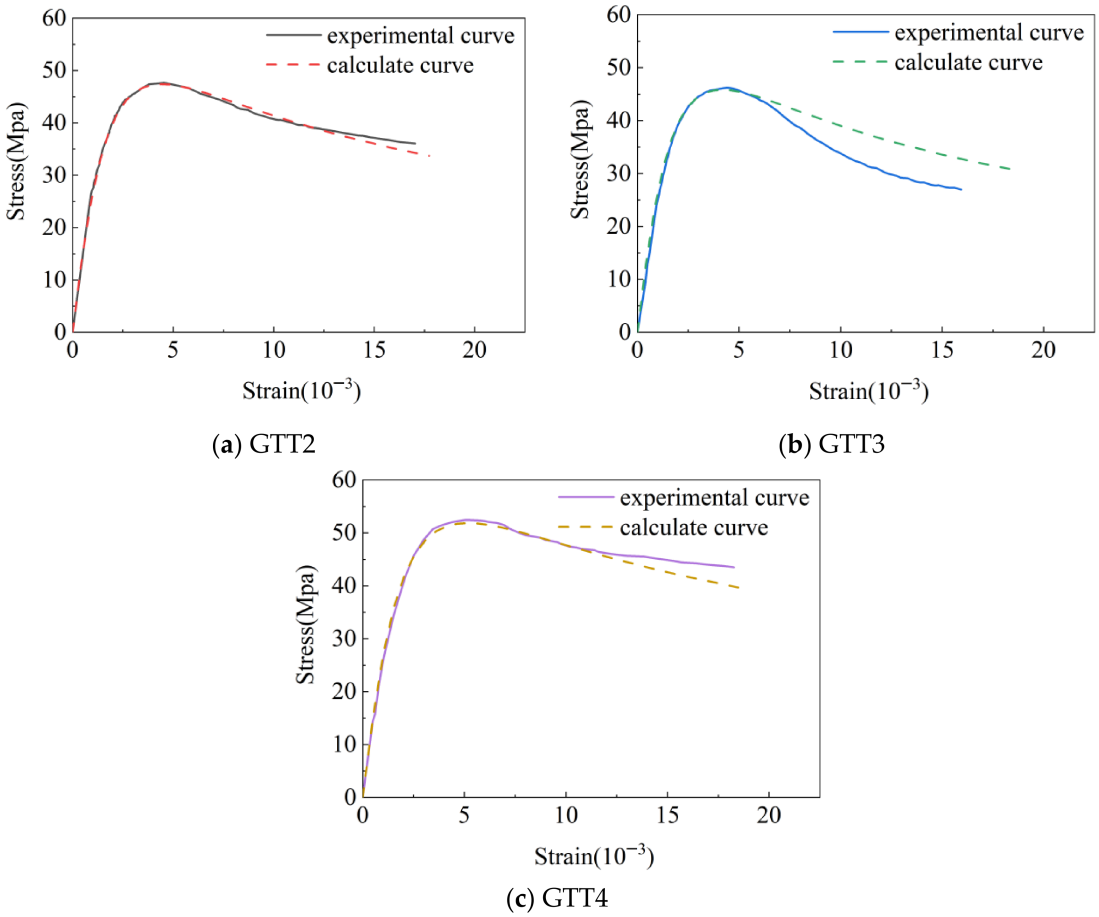

Figure 20. Comparison of experimental and theoretical stress–strain curves.

6. Limitations of the Study

This study provides a foundational stress–strain model for C-shaped steel tube-confined concrete; however, several limitations should be acknowledged:

1. Scale and Number of Datasets: The experimental program comprised four groups with a total of twelve specimens. While this is sufficient to identify key behavioral trends and calibrate the proposed model, the limited number of test datasets may affect the statistical robustness and generalizability of the model across a wider range of geometric and material parameters. Future research will aim to expand the experimental database by conducting tests with varied width-to-thickness ratios, concrete grades, and reinforcement detailing.

2. Independent Validation: To the best of the authors' knowledge, the specific C-shaped tube configuration with three steel plates and one reinforced side has not been previously investigated experimentally by other researchers. Consequently, independent datasets for direct model validation are currently unavailable in the literature. As this structural detail gains more engineering applications, collaboration with other research groups will be pursued to validate and refine the model using newly emerging test data.

3. Loading Condition: The tests were conducted under monotonic axial compression. The behavior under cyclic loading, which is critical for seismic performance assessment of composite shear walls, remains to be investigated.

4. Specimen Scale: The specimens were of relatively small scale (300 mm height). The applicability of the proposed model to full-scale boundary elements requires further verification.

7. Conclusions

Based on the experimental results and theoretical analysis, the following conclusions can be drawn:

1. Test observations indicate that GTT1 (without reinforcement) provides insufficient confinement and is not recommended for engineering practice. GTT2-GTT4 significantly improve concrete ductility. Comparing GTT2 and GTT4 shows that thicker steel plates enhance confinement, leading to higher peak stress, higher peak strain, and better ductility of the confined core concrete. Comparing GTT2 and GTT3 shows that smaller reinforcement spacing enhances confinement, resulting in higher peak stress, higher peak strain, and better ductility. This quantitative relationship provides a direct design reference for detailing the reinforcement in C-shaped boundary elements of composite shear walls.

2. A finite element model of GTT2 was established in ABAQUS 2020and subjected to monotonic axial loading. The reliability of the FE model was verified by comparing the simulated and experimental load–displacement curves. Analysis of the principal stresses in the core concrete validated the assumed effectively confined area for the C-shaped tube.

3. Static equilibrium equations were used to analyze the steel tube, calculating the lateral confining stresses on the concrete. A method for calculating the effective confining stress on the core concrete was proposed. Regression analysis of the experimental peak stresses in the steel plates against the width-to-thickness ratio yielded a calculation method for the plate stress. Regression analysis of the experimental peak strains against the calculated peak stresses yielded a calculation method for the peak strain of C-shaped steel tube-confined concrete.

4. Based on the Mander model and research on square CFST columns, a calculation method for the stress–strain relationship of C-shaped steel tube-confined concrete was proposed. This model offers a significant contribution to the literature by providing the first validated constitutive relationship for this specific C-shaped configuration. It can be directly implemented into fiber-based finite element software (e.g., OpenSees or ABAQUS user material subroutines) to enable more accurate seismic performance simulations of C-shaped steel frame composite shear wall systems, thereby supporting performance-based design methodologies.

Author Contributions: Formal analysis, T.Z.; Data curation, L.Z.; Writing—review & editing, X.M.; Visualization, C.W.; Project administration, D.L. All authors have read and agreed to the published version of the manuscript.

Funding: This research was funded by the Teaching Reform Project of the Jiangxi Provincial Department of Education, grant number JXJG-25-51-22, under the project titled "Research on the Reconstruction and Practice of the 'AI+' Teaching System for Intelligent Construction in Higher Vocational Education-From the Perspective of Industry-University-Research Integration".

Data Availability Statement: The original contributions presented in the study are included in the article, further inquiries can be directed to the corresponding author.

Conflicts of Interest: The authors declare no conflict of interest.

References

1. Srinivasan, C.N.; Schneider, S.P. Axially loaded concrete-filled steel tubes. *J. Struct. Eng.* **1999**, *125*, 1202–1206. [CrossRef]
2. Cai, J.; Long, Y.L. Constitutive relationship of rectangular CFT columns with binding bars. *Eng. Mech.* **2008**, *25*, 137–143. (In Chinese)
3. Guo, X.P. Constitutive relationship of concrete core confined by rectangular steel tube. *Hunan Commun. Sci. Technol.* **2011**, *37*, 74–79. (In Chinese)
4. Feng, P.; Cheng, S.; Bai, Y. Mechanical behavior of concrete-filled square steel tube with FRP-confined concrete core subjected to axial compression. *Compos. Struct.* **2015**, *123*, 312–324. [CrossRef]

5. Katwal, U.; Tao, Z.; Hassan, M.K. Simplified numerical modelling of circular concrete-filled steel tubular stub columns. In *Mechanics of Structures and Materials, Advancements and Challenges*; CRC Press: Boca Raton, FL, USA, 2016; pp. 223–230.
6. Mander, J.B.; Priestley, M.J.N.; Park, R. Observed stress-strain behavior of confined concrete. *J. Struct. Eng.* **1987**, *114*, 1827–1849. [CrossRef]
7. Mander, J.B.; Priestley, M.J.N.; Park, R. Theoretical stress-strain model for confined concrete. *J. Struct. Eng.* **1988**, *114*, 1804–1826. [CrossRef]
8. Xiao, Y.; Tomii, M.; Sakino, K. Experimental study on the design method to prevent the shear failure of reinforced concrete short circular columns by confining in steel tube. *Trans. Jpn. Concr. Inst.* **1986**, *8*, 535–542.
9. Zhang, S.M.; Liu, J.P.; Ma, L.; Xing, T. Axial compression test and analysis of circular tube confined HSC stub columns. *China Civ. Eng. J.* **2007**, *40*, 24–31.
10. Zhou, X.H.; Gan, D.; Liu, J.P.; Zhang, S.M. Experimental study and analysis on square steel tube confined reinforced concrete short columns under axial compression. *J. Build. Struct.* **2011**, *32*, 68–74. (In Chinese)
11. Gao, L.; Zhou, M.; Gao, Y.; Huang, Z.M. Stress-strain relationship of rectangular steel tube confined concrete under axial compression. *J. Civ. Archit. Environ. Eng.* **2018**, *40*, 102–109. (In Chinese)
12. Sargin, M. *Stress-Strain Relationship for Concrete and the Analysis of Structural Concrete Sections*; University of Waterloo: Waterloo, ON, USA, 1968.
13. Saenz, L.P. Discussion of equation for the stress-strain curve of concrete by Desayi and Krishnan. *ACI Mater. J.* **1964**, *61*, 1229–1235.
14. Kent, D.C.; Park, R. Flexural members with confined concrete. *J. Struct. Div.* **1971**, *97*, 1969–1990. [CrossRef]
15. Popovics, S. A numerical approach to the complete stress-strain curve of concrete. *Cem. Concr. Res.* **1973**, *3*, 583–599. [CrossRef]
16. Attard, M.M.; Setunge, S. Stress-strain relationship of confined and unconfined concrete. *ACI Mater. J.* **1996**, *93*, 432–441. [CrossRef] [PubMed]
17. Han, L.H. *Concrete Filled Steel Tube Structures—Theory and Practice*; Science Press: Beijing, China, 2016; pp. 101–118. (In Chinese)
18. Hany, N.F.; Hantouche, E.G.; Harajli, M.H. Axial stress-strain model of CFRP-confined concrete under monotonic and cyclic loading. *J. Compos. Constr.* **2015**, *19*, 04015004. [CrossRef]
19. Lu, Y.; Li, N.; Li, S.; Liang, H. Behavior of steel fiber reinforced concrete-filled steel tube columns under axial compression. *Constr. Build. Mater.* **2015**, *95*, 74–85. (In Chinese) [CrossRef]
20. Shirmohammadi, F.; Esmaeily, A.; Kiaeipour, Z. Stress-strain model for circular concrete columns confined by FRP and conventional lateral steel. *Eng. Struct.* **2015**, *84*, 395–405. [CrossRef]
21. Ziaadiny, H.; Abbasnia, R. Unified cyclic stress strain model for FRP-confined concrete circular, square and rectangular prisms. *Struct. Concr.* **2016**, *17*, 220–234. [CrossRef]
22. Afifi, M.Z.; Mohamed, H.M.; Benmokrane, B. Theoretical stress-strain model for circular concrete columns confined by GFRP spirals and hoops. *Eng. Struct.* **2015**, *102*, 202–213. [CrossRef]
23. *GB/T 2975-2018*; Steel and Steel Products- Location and Preparation of Test Samples for Mechanical Testing. China Architecture & Building Press: Beijing, China, 2018. (In Chinese)
24. *GB/T 228.1-2010*; Metallic Materials-Tensile Testing-Part 1: Method of Test at Room Temperature. China Architecture & Building Press: Beijing, China, 2010. (In Chinese)
25. *GB/T 50081-2019*; Standard for Test Methods of Concrete Physical and Mechanical Properties. China Architecture & Building Press: Beijing, China, 2019. (In Chinese)
26. *GB 50010-2010*; Code for Design of Concrete Structures (2015 Edition). China Architecture & Building Press: Beijing, China, 2015. (In Chinese)

Disclaimer/Publisher's Note: The statements, opinions and data contained in all publications are solely those of the individual author(s) and contributor(s) and not of MDPI and/or the editor(s). MDPI and/or the editor(s) disclaim responsibility for any injury to people or property resulting from any ideas, methods, instructions or products referred to in the content.